JGR Solid Earth

RESEARCH ARTICLE
10.1029/2019JB017512

This article is a companion to Gallovič et al. (2019), http://doi.org/10.1029/2019JB017510.

Key Points:
- We apply a new Bayesian dynamic source inversion to the 2016 Amatrice, Italy, earthquake to infer initial stresses and friction properties
- Ensemble solutions exhibit complex rupture propagation including transient nucleation and pulse-like behavior with low radiation efficiency
- The inferred heterogeneous dynamic models fit very well waveforms recorded at uniquely dense network of near-source seismic stations

Correspondence to:
F. Gallovič,
gallovic@karel.troja.mff.cuni.cz

Citation:
Gallovič, F., Valentová, Ľ., Ampuero, J.-P., & Gabriel, A.-A. (2019). Bayesian dynamic finite-fault inversion: 2. Application to the 2016 M_w 6.2 Amatrice, Italy, earthquake. *Journal of Geophysical Research: Solid Earth*, *124*, 6970–6988. https://doi.org/10.1029/2019JB017512

Received 7 FEB 2019
Accepted 19 JUN 2019
Accepted article online 3 JUL 2019
Published online 22 JUL 2019

©2019. American Geophysical Union. All Rights Reserved.

Bayesian Dynamic Finite-Fault Inversion: 2. Application to the 2016 M_w 6.2 Amatrice, Italy, Earthquake

F. Gallovič[1], Ľ. Valentová[1], J.-P. Ampuero[2], and A.-A. Gabriel[3]

[1]Faculty of Mathematics and Physics, Department of Geophysics, Charles University, Prague, Czech Republic, [2]Université Cote d'Azur, IRD, CNRS, Observatoire de la Cote d'Azur, Géoazur, Sophia Antipolis, France, [3]Geophysics, Department of Earth and Environmental Sciences, Ludwig-Maximilians-Universität München, Munich, Germany

Abstract In 2016 Central Italy was struck by a sequence of three normal-faulting earthquakes with moment magnitude (M_w) larger than 6. The M_w 6.2 Amatrice event (24 August) was the first one, causing building collapse and about 300 casualties. The event was recorded by a uniquely dense network of seismic stations. Here we perform its dynamic source inversion to infer the fault friction parameters and stress conditions that controlled the earthquake rupture. We consider a linear slip-weakening friction law with spatially variable parameters along the fault. The inversion uses a novel Bayesian framework developed in our companion paper, which combines efficient finite-difference dynamic rupture simulations and the Parallel Tempering Monte Carlo algorithm to sample the posterior probability density function. The main advantage of such formulation is that by subsequent analysis of the posterior samples we can infer stable features of the result and their uncertainty. The inversion results in a million of visited models. The preferred model ensemble reveals intriguing dynamic features. The rupture exhibits a slow and irregular nucleation followed by bilateral rupture propagation through two asperities, accelerating toward the heavily damaged city of Amatrice. The stress drop reaches locally 10–15 MPa, with slip-weighted mean of 4–4.5 MPa. The friction drop ranges from 0.1 to 0.4. The characteristic slip-weakening distance is the most heterogeneously distributed dynamic parameter, with values of 0.2–0.8 m. The radiation efficiency was rather low, 0.2, suggesting that approximately 80% of the total available energy was spent in the fracture process, while just 20% was radiated by seismic waves.

1. Introduction

In 2016 Central Italy was struck by three $M_w > 6$ earthquakes associated with normal faulting with NW-SE strike and dip toward SW, which is the prevalent style of faulting in the area (Chiaraluce et al., 2017). The first strong earthquake of the sequence (24 August, M_w 6.2) caused building collapse and about 300 casualties. Two months later, the next event (26 October, M_w 6.1) extended the seismogenic volume to the NW, and 4 days later (30 October, M_w 6.5) the largest event hit the same area. The events were recorded by a uniquely dense network of near-source seismic stations. Kinematic source inversion of all the three events by Pizzi et al. (2017) using the method by Gallovič et al. (2015) suggests complementarity of their ruptures with possible relations to the growth of the normal fault system in the area. Aochi and Twardzik (2019) performed an iterative search for dynamic rupture parameters of two seismogenic asperities by comparison with near-field ground motions. Other (kinematic) finite-fault source inversion models (e.g., Cheloni et al., 2017; Cirella et al., 2018; Tinti et al., 2016) based on geological, geodetic, and seismic data reveal a rather large degree of nonuniqueness, which is typical of ill-constrained source inversion problems.

Kinematic source inversions, which infer the coseismic slip history along the fault, provide only limited information on the physical processes driving the rupture. Instead, dynamic source inversion is a systematic approach by which the distributions of stress and parameters of an assumed friction law along the fault are optimized so that the resulting dynamic rupture model produces ground motions that fit the observed data. Earthquake dynamic modeling is a key element for understanding the physics of earthquake occurrence, nucleation, propagation, and arrest. In the last decades there has been substantial progress in dynamic rupture modeling, so that recent studies of selected earthquakes have shed new light on earthquake processes (e.g., Ulrich et al., 2019). Nevertheless, just few attempts of full dynamic source inversion have been made so far (Corish et al., 2007; Fukuyama & Mikumo, 1993; Peyrat & Olsen, 2004) due to its high computational burden.

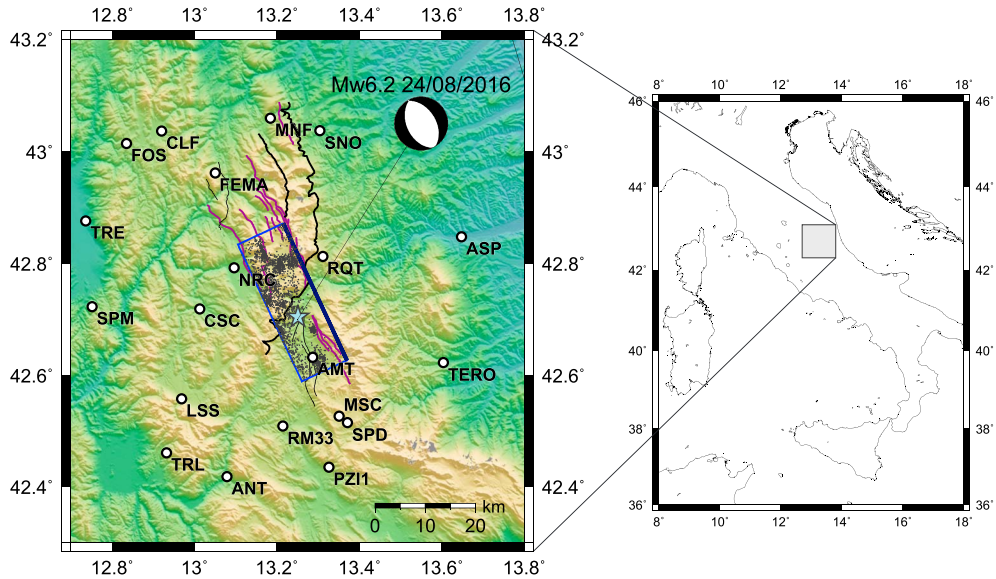

Figure 1. Map of Italy (right) with zoomed-in epicentral area of the 2016 Amatrice earthquake (left). The fault plane adopted from Pizzi et al. (2017) is shown by the rectangle (the thick line corresponds to the top edge at the surface). Stations are shown by white circles. The INGV mechanism and centroid location is shown by the beach ball. Mainshock epicenter (light blue star) and on-fault aftershocks (gray dots) are taken from the relocated catalog by Chiaraluce et al. (2017). Black and red curves correspond to Miocene-Pliocene thrusts and active normal faults, respectively.

In our companion paper (Gallovič et al., 2019) we introduce a novel Bayesian dynamic source inversion method. Here we apply it to infer physical parameters and stress conditions that governed the 2016 M_w 6.2 Amatrice earthquake. We adopt the fault geometry assumed by Pizzi et al. (2017). We consider a heterogeneous prestress and a linear slip-weakening friction law parameterized by along-fault distributions of the difference between static and dynamic friction coefficients (friction drop) and slip-weakening distance D_c. The spatial distributions of those parameters are determined by a Monte Carlo Markov Chain (MCMC) approach in a nonlinear dynamic inversion that aims at fitting displacement waveforms at 20 stations within 50-km fault distance (Figure 1) at frequencies lower than 1 Hz. After discussing the inversion results, we simulate the wavefield at frequencies up to 5 Hz, demonstrating that the main features of the observed velocity waveforms are captured by the synthetics, especially at stations where site effects are presumably insignificant.

2. Method

Here we give an overview of the main features of the Bayesian dynamic source inversion introduced in our companion paper. Therein, the approach is validated on a community benchmark test based on a spontaneous dynamic rupture model (Mai et al., 2016).

We assume a planar fault governed by the linear slip-weakening friction law (Figure 2a) embedded in an elastic medium. The 3-D elastodynamic equation and dynamic rupture are solved in a relatively small box covering the fault using a finite difference method (code FD3D by Madariaga et al., 1998, with thin fault boundary conditions; Ruiz & Madariaga, 2011; Twardzik et al., 2014). The computational box can be made small because we do not need to include the station; the station waveforms are calculated externally as specified further. Pure dip slip on a vertical fault is considered for computational efficiency. A one-dimensional layered elastic velocity structure is assumed (Figure 3). The variable model parameters (initial stress, friction drop, and D_c) are parameterized by values on control points covering the fault (Figure 2c), from which they are bilinearly interpolated onto the denser finite-difference (FD) computational grid (for the actual grid size values see Table 1). The dynamic simulation results in slip rate histories along the fault. Following the seismological representation theorem (Aki & Richards, 2002), the slip rate functions are then convolved with Green's functions representing impulse responses of the medium. The Green's functions are precalculated at stations inside and outside the finite-difference domain using a different method and software, Axitra (Bouchon, 1981; Coutant, 1989; Kennett & Kerry, 1979). It is based on the discrete wave number and

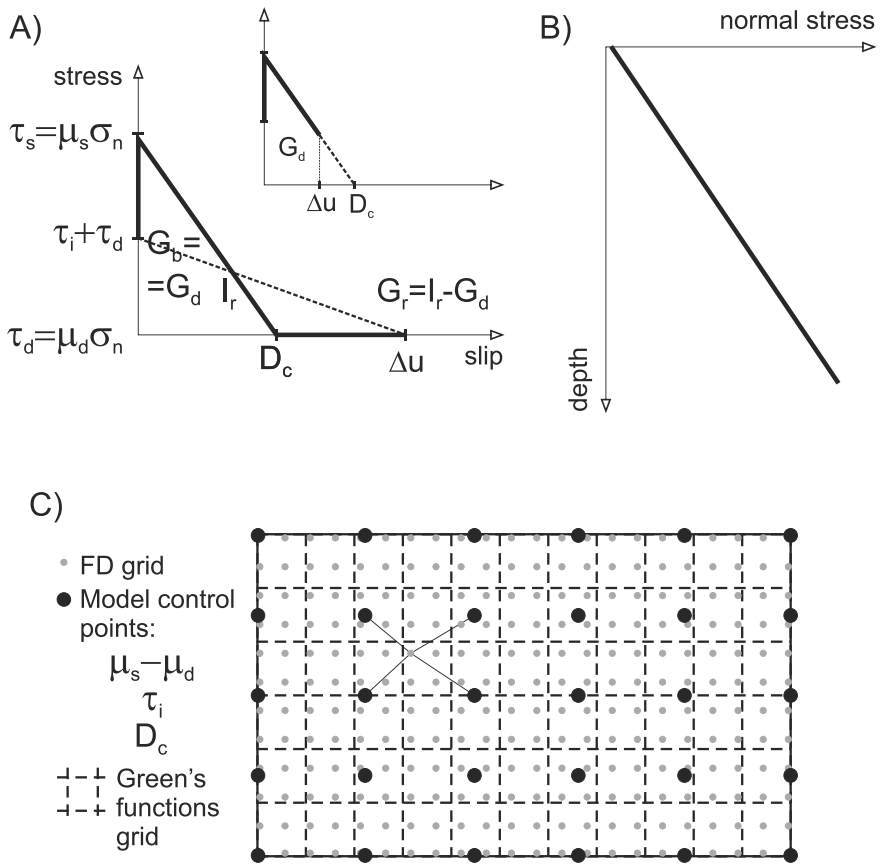

Figure 2. Rupture model and its parameterization. (a) Linear slip-weakening friction law. Inverted parameters are prestress (initial stress) τ_i, difference between static and dynamic friction coefficients (μ_s–μ_d), and characteristic slip-weakening distance D_c. The frictional coefficient difference is converted to the respective breakdown stress drop by multiplication with a prescribed normal stress depth profile (b). G_b, G_d, and G_r are breakdown, dissipated breakdown, and radiated energy densities (Kanamori & Brodsky, 2004, see text). Note that G_r is calculated as the difference between the dashed triangle and G_d. The inset illustrates situation when the slip does not reach D_c, that is, when the breakdown work and dissipated energies differ. (c) Illustration of three grids considered in the modeling. Model parameters are defined on the coarsest grid of control points. The values are bilinearly interpolated onto the densest finite-difference (FD) grid that is used by the FD3D dynamic rupture simulations. Slip rates calculated by FD3D are averaged spatially onto the coarser Green's functions grid, for which Green's functions are precalculated and stored. Waveforms are calculated by convolving the individual averaged slip rates with the respective Green's functions and summed, following the representation theorem. For the actual grid parameters considered in the present study see Table 1.

matrix methods, adopting the correct (dipping) fault geometry. As a result, synthetic seismograms at specified stations are obtained. The misfit relative to observations is evaluated as the weighted L2 norm of the difference between observed and simulated displacement waveforms after applying the same, optimal time shift uniformly to all stations and components.

While the use of a vertical fault in the dynamic rupture simulation seems a very crude approximation of the actual 45° dipping fault geometry, this approximation affects only the dynamic rupture simulation and not the calculation of synthetic seismograms. We have tested the validity of our approximation by comparing rupture propagation simulations by FD3D and WaveQLab3D (Duru & Dunham, 2016) that uses summation-by-parts (SBP) sixth-order finite difference operators on boundary-conforming curvilinear mesh, thus accounting for the fault dip. Both methods include free surface boundary condition. As shown in Appendix A for our best-fitting model, the rupture models and generated seismograms agree sufficiently well. For more discussion on this point see Appendix A.

Model optimization is performed using the MCMC method called Parallel Tempering (e.g., Falcioni & Deem, 1999; Sambridge, 2013). The method is similar to the classical simulated annealing, as the

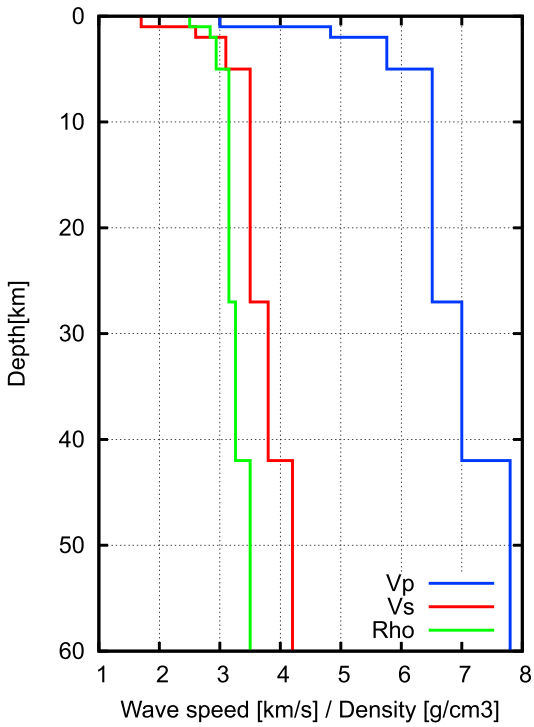

Figure 3. Velocity and density depth profile considered both in dynamic rupture simulations and waveform calculations (Green's functions). Adopted from Ameri et al. (2012).

posterior probability density function (PDF) is modified by a temperature T. Instead of a gradual decrease in T, the Parallel Tempering method employs a set of Markov chains simultaneously advancing at various temperatures. To ensure sufficient sampling of the model space, the chains are allowed to exchange temperature values following the adapted Metropolis-Hastings acceptance rule (Sambridge, 2013). This way, we obtain samples of the posterior PDF function, whose parameters can be further analyzed in a statistical sense.

3. Data, Velocity Model, and Fault Geometry

We use strong motion data recorded by the Rete Accelerometrica Nazionale and the Rete Sismometrica Nazionale, operated by the Italian Department of Civil Protection and the Istituto Nazionale di Geofisica e Vulcanologia, respectively. The records were downloaded from the Engineering Strong-Motion database (Luzi, Puglia, Russo, D'Amico, et al., 2016; Luzi, Puglia, Russo, & ORFEUS WG5, 2016). For the inversion we use all 20 three-component strong motion waveforms recorded within 50 km from the fault.

We filtered the data by a fourth-order causal Butterworth filter between 0.05 and 1 Hz for the closest stations AMT and NRC, and between 0.05 and 0.5 Hz for the other stations (with the exception of station RQT where the 0.1- to 0.5-Hz band was considered). The high-pass filtering removes low-frequency (mostly instrumental) noise from the data, while the low-pass filter is dictated by limitations of our synthetic Green's functions due to imperfect velocity model (Hallo & Gallovič, 2016) and imprecise location and geometry of the fault (Ragon et al., 2018, 2019). The waveforms are not weighted; implicitly, the station weights are given by the recorded amplitudes, which are higher at the closest stations. We consider that the data error standard deviation is equal to 0.1 m, which

Table 1
Model and Computational Parameters Considered for the 2016 Amatrice Earthquake

Parameter	Value
General	
Fault mechanism	Strike: 155°, dip: 45°, rake: −85°
Fault dimensions	Length 30 km, width 14 km
Fault top depth	0 km
Normal stress depth gradient	8.5 MPa/km
FD3D	
Spatial discretization	0.1 km
FD half-domain size (along strike × normal × along dip)	300 × 100 × 140
Duration of slip rate functions	10 s
Time step	0.002 s
Green's functions	
Spatial fault discretization	0.5 × 0.5 km
Time sampling	0.2 s
Waveform frequency range (displacements)	0.05–1.0 Hz (AMT, NRC) 0.05–0.5 Hz (other stations)
Model parameterization and prior ranges of parameters (homogeneous along the fault)	
Control point grid (along-strike × along-dip)	13 x 8
Prestress prior	0 – 100 MPa
Static-Dynamic friction coefficient prior	0 – 1.1
Characteristic slip-weakening distance prior	0.15 – 1.00 m
Nucleation area prior (along-strike, up-dip, radius)	16 km, 7 km, 4 km

is twice larger than that considered by Pizzi et al. (2017), to account for the uncertainty of the velocity model, fault geometry, and also for inaccuracies of the dynamic simulation method.

The causative fault plane of the Amatrice earthquake was thoroughly investigated by Tung and Masterlark (2018). Using static 3-D finite-element modeling, they found that a listric fault geometry provides the best fit of the observed InSAR data. Nevertheless, due to limitations of the forward solver we use a planar fault inferred from seismological data by Pizzi et al. (2017) by kinematic finite-fault inversion with grid search over the fault plane location, fault geometry (strike and dip), and slip direction (rake). To reduce the computational cost, we slightly adjusted the size of the optimal fault by Pizzi et al. (2017) from 36×12 to 30×14 km.

Synthetic Green's functions are calculated for the 1-D velocity model (Figure 3) adopted from Gallovič and Zahradník (2012) and Ameri et al. (2012), who used it for low-frequency and broadband modeling of the 2009 L'Aquila earthquake, respectively. This velocity model was also used by Pizzi et al. (2017) for the kinematic inversion of the 2018 Amatrice earthquake. The Green's functions (and thus the synthetics) are filtered in the same way as the data for consistency.

4. Dynamic Inversion Setup and Strategy

The grid parameters and normal stress profile considered in the present study are listed in Table 1, along with a priori bounds on the values of the dynamic parameters. In addition, since we have prior approximate information about the hypocenter position, each newly proposed model in the MCMC sampling is allowed to have negative strength excess (the difference between static frictional strength and initial shear stress) only in a prescribed nucleation area (see Table 1). Any model that violates this condition is discarded and a new proposal model is generated without running an expensive dynamic simulation. In the dynamic simulations the negative strength excess area initiates the rupture propagation. Depending on dynamic parameters within and around this initial patch, the rupture may or may not continue to propagate outside the nucleation area in a spontaneous matter.

Regarding the initial model for the dynamic inversion, we explain in the companion paper that the MCMC sampling cannot start from very random models, because the sampling would require an unbearable amount of trial dynamic rupture simulations to find the proper part of the model space with meaningful rupture models. Indeed, in most of the model space the rupture would not even start or would start, but in an unsuitable manner (e.g., unilateral, too fast or slow or with incorrect seismic moment) resulting in poor fit to the data. To avoid this, we follow the strategy outlined in the companion paper, combining prior information on the nucleation area and using a starting model based on a preliminary kinematic slip inversion as detailed below.

We build the initial model from the slip model determined by linear kinematic source inversion using the code LinSlipInv (Gallovič et al., 2015) as in Pizzi et al. (2017). The stress drop distribution is computed from the final slip distribution using the elastostatic formulas for dislocations in a homogenous half space by Okada (1992). The initial stress is set equal to the dynamic frictional strength plus the resulting stress drop. The other dynamic parameters are set manually to obtain a rupture model with positive variance reduction (VR). Achieving that required to prevent the rupture from reaching the surface (which would largely overestimate ground motions) by setting larger values of the static friction and D_c in the upper ~5 km. We also limited the rupture depth by prescribing larger values of the dynamic parameters at the bottom of the fault. We used the parallel tempering inversion to improve this dynamic model in terms of waveform fit. In the inversion even the previously prescribed values at shallow depths and fault edges are allowed to change. During this procedure we stopped the inversion several times, selected the best-fitting model, and used it as a new starting model. In some cases we also manually changed dynamic parameters to improve the fit especially at the closest stations, thus guiding the Monte Carlo sampler to reach faster the part of the model space with well-fitting rupture models. For example, we increased the prestress of the SE asperity and decreased D_c to increase the slip and rupture speed, which in turn amplifies waveform amplitudes at the AMT station; the inversion was then rerun. Once VR exceeded ~0.5, we started the final extensive exploitation of the model space that resulted in the ensemble of posterior samples investigated in the next section.

In the exploitation phase we used in total ~10,000 MCMC chains (with about one fifth at temperature $T = 1$) that visited ~1,000,000 models. Every tenth step of the Markov chain the models at $T = 1$ were saved. The final set consists of ~5,000 model samples representing the random draws from the posterior PDF. In all

the calculations we combined runs on the Xeon supercomputer cluster IT4I and our local farm of 10 graphics processing unit (GPU) cards.

5. Results

In the following we discuss first the properties of the best-fitting model (maximum likelihood estimate) to give an idea about the rupture properties, waveform fit, and the controlling dynamic parameters. Then, since the inversion result is to be understood in the Bayesian framework as a family of solutions, we discuss uncertainties of both kinematic and dynamic parameters of the sampled posterior PDF.

5.1. Best-Model Properties

Figure 4a displays the slip distribution and slip rate functions of the best-fitting dynamic rupture model with variance reduction VR = 0.62. The slip rate snapshots showing the rupture evolution in time are presented in Figure 4b. Figure 5 shows along-fault distributions of the stress drop, rupture time, rupture speed, and rise time (calculated as a ratio of final slip and peak slip rate). In agreement with published kinematic rupture models, our best-fitting dynamic model exhibits a bilateral rupture propagation with very weak nucleation. Indeed, during the first 2–3 s the rupture almost ceases and is followed by a fast recovery of the spontaneous rupture process. The rupture propagates first toward the SE at relatively high speed and with short rise times (Figure 5). During this period, the rupture propagates at smaller speed, smaller peak slip rates, and with longer rise times also toward the NW. Before stopping in the SE direction, the NW part of the rupture accelerates, increasing the peak slip rates and shortening the rise times. The largest slip is located in the NW part of the fault. The major slip area is depleted of on-fault aftershocks, consistent with stress release.

In Figure 4c we compare synthetic and observed displacement waveforms. The highest amplitudes observed at station AMT, well fitted by our model, are related to the energetic rupture propagation toward the site, suggesting a strong directivity effect. Contrarily, at the other nearest station, NRC, the waveform fit is not so good, perhaps due to the simplification of the fault geometry, which affects more strongly the nearest stations. For the remaining, more distant stations the waveform fit is excellent.

Figure 6 shows the dynamic parameters of this particular source model. Note that dynamic parameters outside the ruptured area (delimited by the black contour in Figure 6) are not constrained by the inversion (see section 5.2). The first two rows of Figure 6 contain the distributions of relative prestress τ_i, friction drop, and D_c. The prestress presented is relative to the dynamic frictional strength of the fault; in the rupture area, it is an estimate of the coseismic stress drop. In particular, the prestress is elongated horizontally, having a maximum of 12 MPa SE of the hypocentral area and two additional minor local maxima of ~7 MPa located further in the NW and SE directions from the nucleation. Within the rupture area the friction drop values range from 0.1 to 0.4. The largest values are located in a profound heterogeneity located close to the hypocenter in the SE direction. The characteristic slip-weakening distance D_c is the most heterogeneously distributed dynamic parameter, with values between 0.2 and 0.8 m. The lowest values of D_c are located in a narrow, horizontally elongated patch, approximately at the middle depth of the rupture. This patch lacks on-fault aftershocks, presumably due to the fact that the stress was released by the mainshock slip.

Next we discuss several derived quantities calculated from the distribution of the inverted dynamic parameters. In particular, the distribution of strength excess ($\tau_s - (\tau_i + \tau_d)$, see Figure 2) displayed in Figure 6 shows that the nucleation region is only weakly overstressed (~ −0.1 MPa). Outside the nucleation area the strength excess is approximately constant, (~4 MPa). The region of large prestress located SE of the hypocenter is thus compensated by a larger strength. The strength excess increases strongly at the edges of the ruptured area to values larger than 10 MPa, which causes the rupture to stop.

The along-strike prolongation of the rupture can be observed also in the distribution of the so-called S parameter, characterizing the on-fault stress state (Andrews, 1976), defined as

$$S = \frac{\tau_s - (\tau_i + \tau_d)}{(\tau_i + \tau_d) - \tau_d} = \frac{(\tau_s - \tau_d) - \tau_i}{\tau_i} = \frac{(\mu_s - \mu_d)\sigma_n - \tau_i}{\tau_i}. \quad (1)$$

For the definition of the stresses and friction coefficients in equation (1) see Figure 2a. The S parameter ranges between 0.1 and 0.4 in a patch much narrower than the rupture extent. We note that for S values

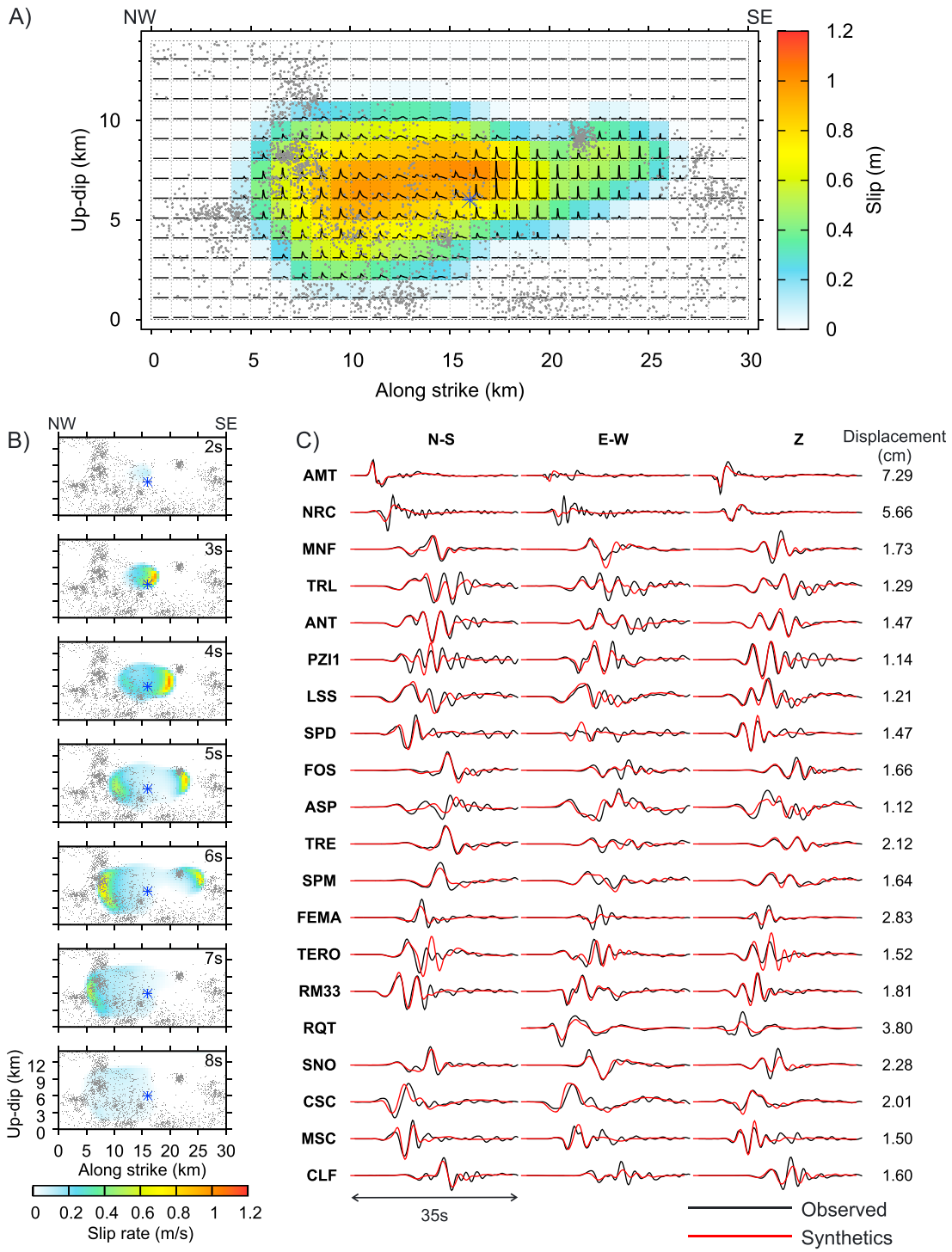

Figure 4. (a) Slip distribution (color coded) with superimposed slip rates of the best-fitting dynamic source model found by our dynamic inversion. Note that here for clarity the dynamic slip rates are shown on 1-km × 1-km grid, which is coarser than actually used in the waveform modeling. Star denotes the location of the hypocenter. (b) Snapshots of slip rates showing the rupture propagation along the fault. Note that within the first 2 s (shown in Figure A1 in Appendix A) the nucleation is so weak that the rupture almost ceases. In panels (a) and (b) the gray points mark the relocated on-fault aftershocks. (c) Comparison between observed and synthetic data for the present model in frequency range 0.05–1.0 Hz (AMT and NRC stations) and 0.05–0.5 Hz (others). The variance reduction is 0.62.

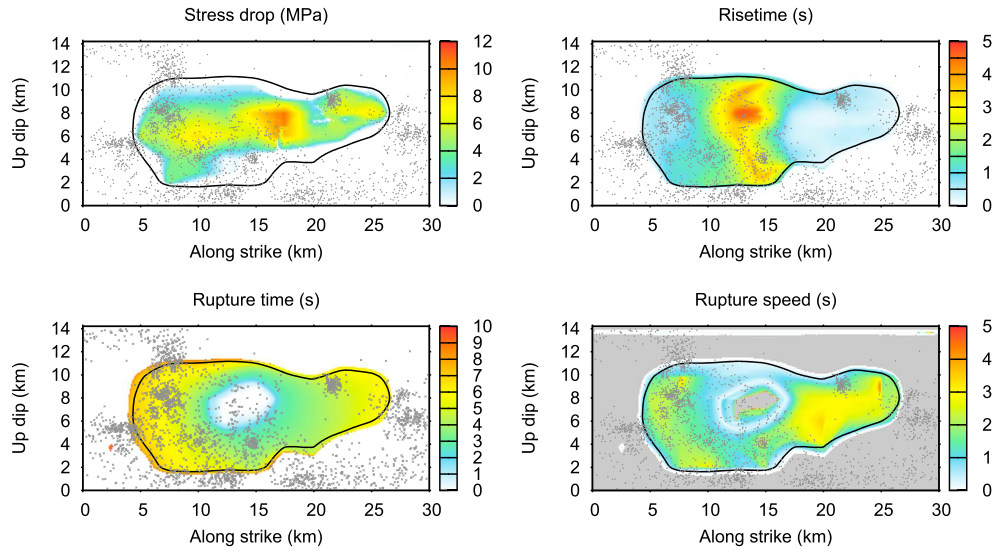

Figure 5. Kinematic parameters of the best-fitting model (see panel titles). Black contours (same in all panels) delineate the slip distribution (see Figure 4a). The gray points show the relocated on-fault aftershocks. The rupture speed (bottom right) is calculated locally from the distribution of rupture times (bottom left); gray masks areas with undetermined values.

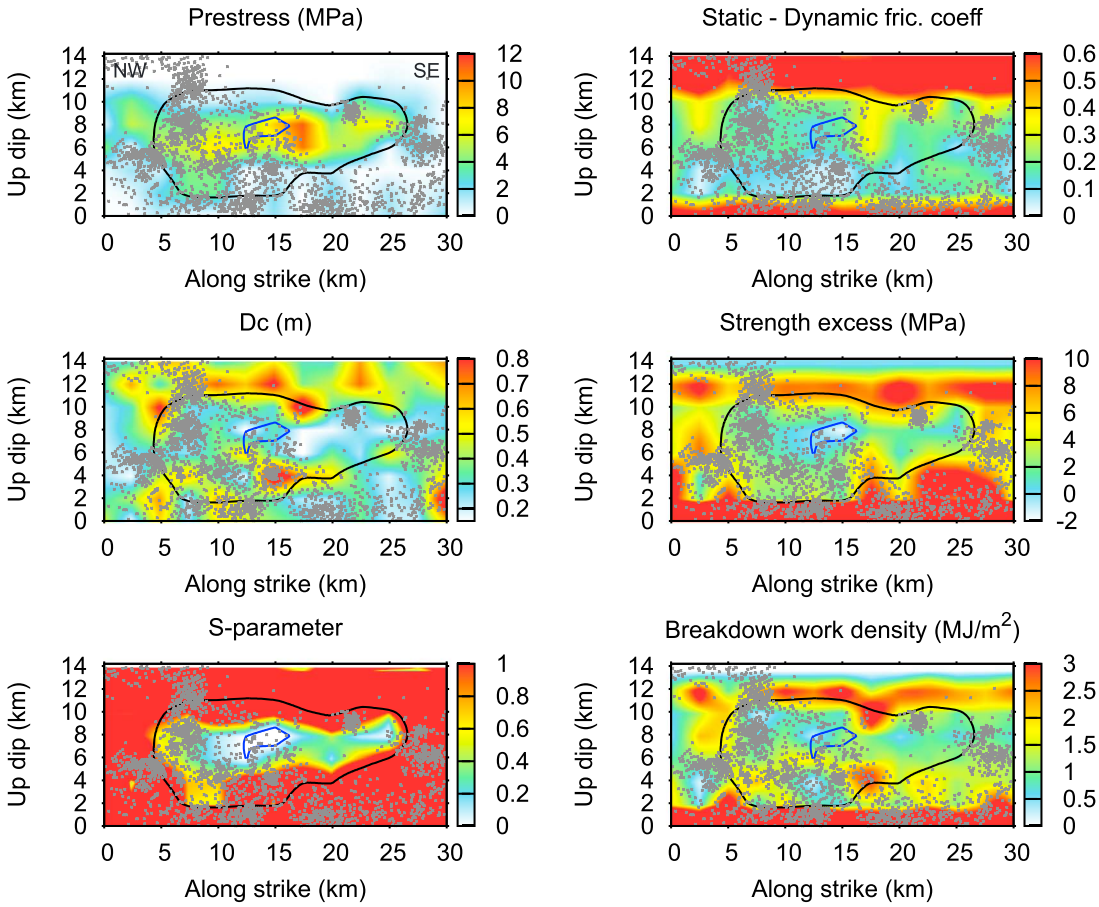

Figure 6. Dynamic parameters of the best-fitting model (see panel titles). Black and blue contours (same in all panels) delineate the slip distribution (see Figure 4a) and nucleation zone (having negative strength excess), respectively. The gray points show the relocated on-fault aftershocks.

as small as 0.1–0.4 the rupture would go supershear on a homogeneous and unbounded fault (Andrews, 1976; Dunham, 2007). However, in our model this behavior is prevented by early stopping (arrest) phases due to the limited width of the rupture (Beroza & Mikumo, 1996; Dunham, 2007). Outside of this patch the S parameter quickly increases to values larger than 1. Nevertheless, the rupture propagates even to those areas but with smaller slip values.

For the best-fitting model Figure 6 also shows the along-fault distributions of breakdown work density, also known as fracture energy, defined in Figure 2 as

$$G_b = \frac{1}{2}(\tau_s - \tau_d)D_c, \tag{2}$$

(Kanamori & Brodsky, 2004; Ripperger et al., 2007). The mean breakdown work density is 1.1 MJ/m^2. This value is comparable to that inferred for past earthquakes of similar magnitude or similar average slip of 0.67 m (Viesca & Garagash, 2015), but the uncertainty of those estimates is large. The total breakdown work (integrated along the fault) is 1.6×10^{14} J.

As discussed in the methodological sections, we use several approximations in the dynamic rupture simulation when performing the inversion. To confirm that the best-fitting model is simulated correctly, we have recalculated it using the more advanced code WaveQLab3D (Duru & Dunham, 2016), a sixth-order accurate finite difference code, which has been verified in many community dynamic rupture benchmarks (Harris et al., 2018). In the WaveQLab3D simulation we respect the actual dipping fault geometry. We present the comparison between the FD3D and WaveQLab3D solutions in terms of slip rates and radiated waveforms in Appendix A1. Compared to our approximate solution, the WaveQLab3D modeling results in only slightly faster rupture propagation, providing slightly larger displacement amplitudes (Figure A1). Nevertheless, in the Bayesian approach the best-fitting model cannot be considered as the closest one to the true model. This is due to the random errors caused by both observational errors and modeling errors due to the use of the fast dynamic solver, as demonstrated on a synthetic test in the companion paper. Instead, the result of the inversion is not one preferred model but an ensemble, the whole set of posterior PDF samples. Therefore, in the following section we analyze statistical properties of the inferred ensemble.

5.2. Ensemble Properties

Figure 7 shows histograms of various parameters derived from the ensemble of rupture models, considering only models with posterior probability density value larger than 2% of the posterior PDF maximum (~5,000 models). The scalar seismic moment covers the value 2.5×10^{18} Nm provided by the Harvard CMT project. The slip-weighted mean stress drop ranges from 4.0 to 4.5 MPa, which falls within the range of stress drops in Central Italy as reported by Bindi et al. (2018) and Pacor et al. (2016). The nucleation zone area spans the range of 2–10 km^2 with mean nucleation overstress up to 1.5 MPa. The total fracture energy E_d and radiated energy E_r calculated according to Ripperger et al. (2007) are of 1.5×10^{14} Nm and 5×10^{13} Nm, respectively. Aochi and Twardzik (2019) inferred ~2 times smaller fracture energy. Nevertheless, they also obtained ~2 times smaller ruptured area, implying that the fracture energy rates are consistent with our rupture ensemble.

The ratio between radiated energy and seismic moment (scaled energy, e.g., Kanamori & Brodsky, 2004) is approximately 1.7×10^{-5} (1.2–2.2×10^{-5}). The radiation efficiency, defined as

$$\eta_r = \frac{E_r}{E_r + E_b}, \tag{5}$$

spans the range of 0.15–0.25, suggesting that approximately 80% of the total available energy was spent in the fracture process, while just 20% was radiated by seismic waves.

Figure 8a shows distributions of mean slip, stress drop, and rise time values along the fault and their uncertainty expressed as twice the standard deviation σ. In all cases the uncertainty is largest at the edge of the rupture (see the black contour of the mean slip in Figure 8a), because the rupture extent varies among the inferred source models. Indeed, the rupture extent variability can be appreciated from Figure 8b, which shows contours of slip of the individual accepted models. Note that some of the models reach the free

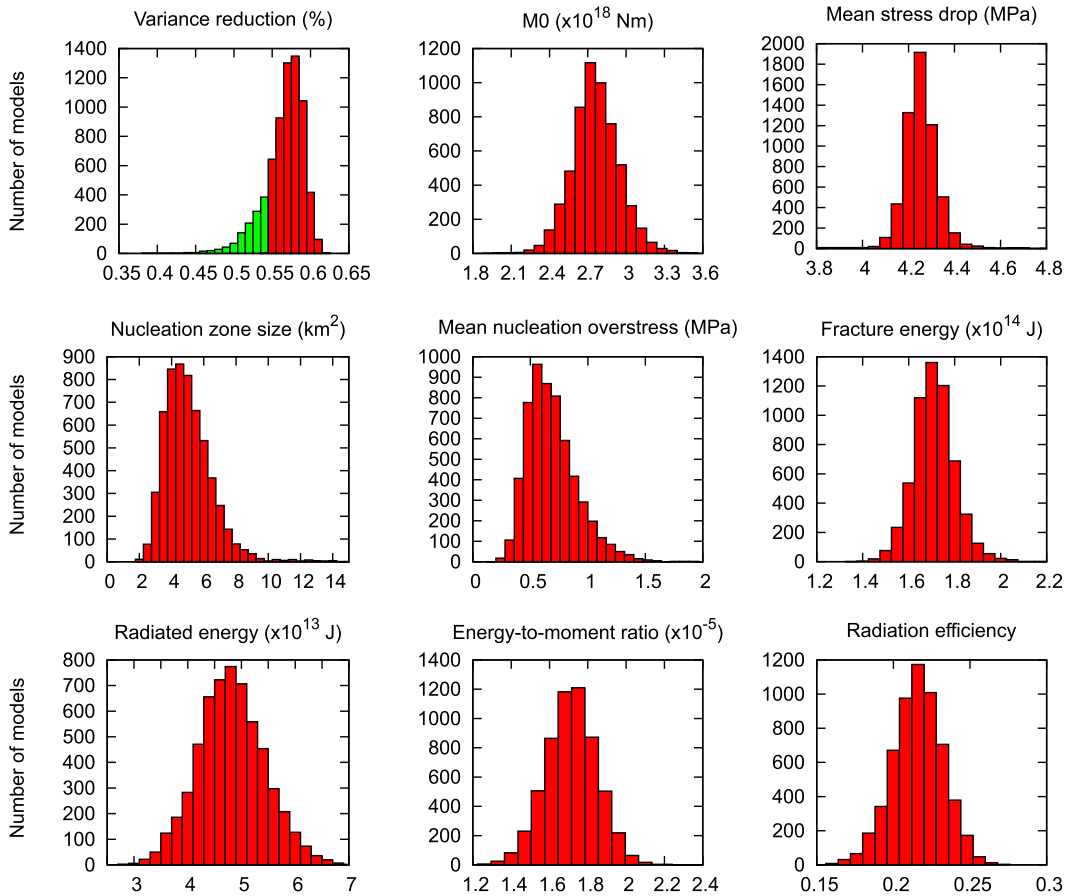

Figure 7. Histograms of rupture parameters (see panel titles) as inferred by our Bayesian inversion considering models having posterior probability density value larger than 2% of the posterior PDF maximum (accepted models, in red). In the top left panel the combined red and green histogram corresponds to the variance reduction of all posterior model samples.

surface, but with rather small slip values. The mean slip has maximum amplitude of ~1.2 m, and its uncertainty reaches 0.1 m, that is, ~10% of the mean. The mean stress drop is ~12 MPa. Its relative variability is around 10% in the middle and NW parts of the fault. It reaches ~20–30% in the SE part of the fault, perhaps because this part of the inferred rupture is strongly controlled by a single nearby AMT station. The rise time distribution suggests that the rupture starts as a crack, with larger rise times (~4 s) in the middle of the fault, and then becomes a pulse, with short rise times (~0.2 s). This result is supported by the uncertainty analysis: the relative variability is around 20% both for the large and short rise times. Notably, rupture speed exhibits overall a comparably large variability of 25%.

Figure 9 shows mean values of dynamic parameters and their scatter in terms of twice the standard deviation σ. The mean values are very close to the values of the best-fitting model (cf. Figure 6). The uncertainties (Figure 9) are irregularly distributed. They have larger values in areas with large mean values, suggesting approximately constant relative uncertainty. The relative standard deviation of prestress and friction drop (and thus strength excess) is approximately 20%, while that of D_c reaches ~50%.

6. Discussion

Our inferred set of models of the 2016 Amatrice earthquake (including the best-fitting model) agrees with published kinematic and dynamic models in a general sense. They exhibit bilateral rupture propagation and have two slip maxima away from the rupture nucleation (Aochi & Twardzik, 2019; Cirella et al., 2018; Pizzi et al., 2017). The latter feature has been also revealed in geodetic inversion by Huang et al.

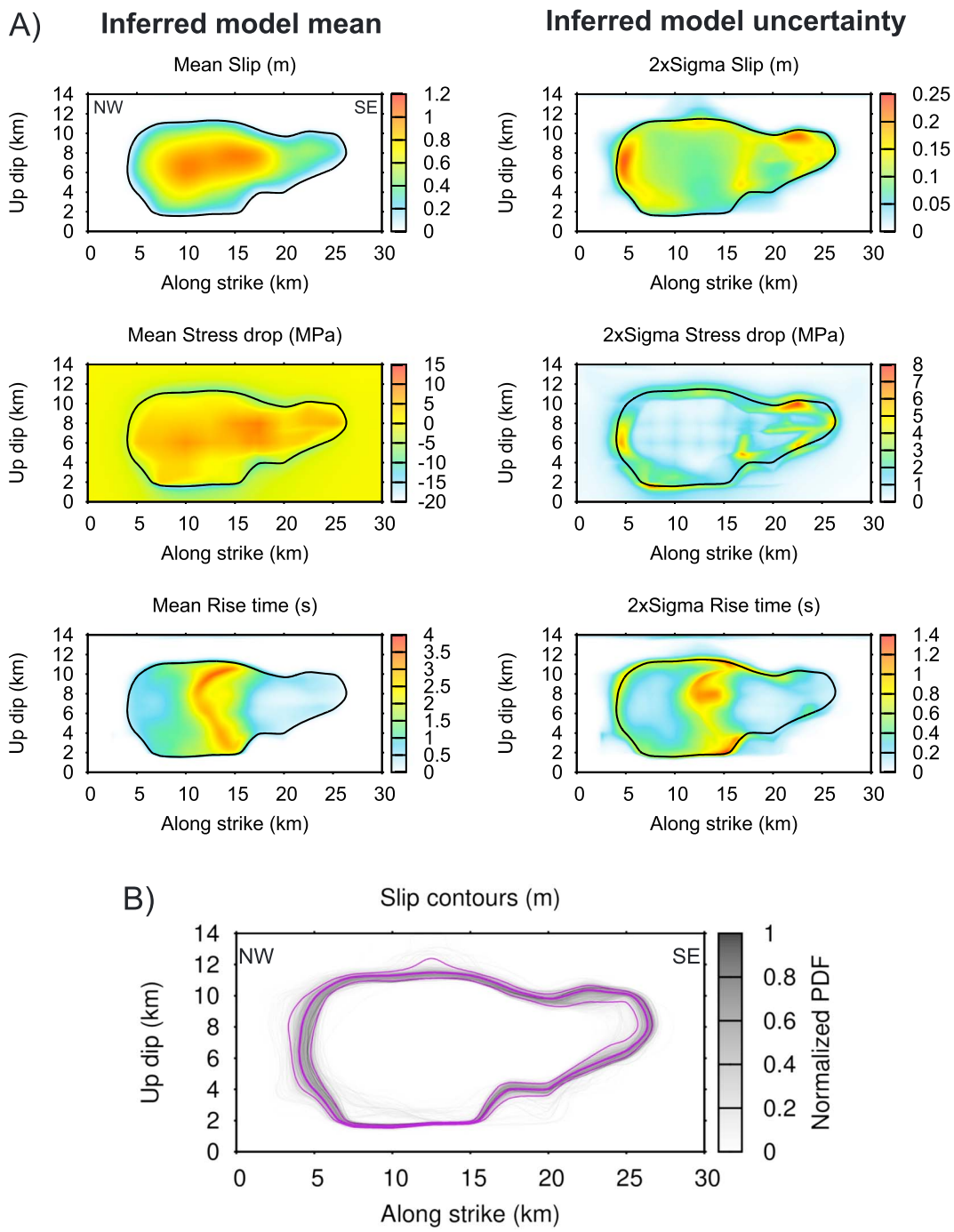

Figure 8. (a) Rupture parameters inferred by the Bayesian dynamic inversion averaged over posterior samples (left) and the model parameters' uncertainty in terms of 2 sigma (right). (b) Slip contours of all accepted posterior model samples coded in gray displaying the variability of the inferred spatial rupture extent. The thick and thin magenta lines show the contours of the averaged slip model and its 2 sigma uncertainty.

(2017). Rupture propagation along the SE portion of the fault contributed to the ground motion amplification in Amatrice, which experienced significant damage and casualties and recorded peak acceleration reaching 0.8 g (Fiorentino et al., 2018). As identified by Ren et al. (2017), at larger distances the directivity effect was dominated by the NW rupture propagation along the spatially larger asperity with larger slip.

Our dynamic models exhibit relatively smooth slip distribution in accord with the models by Pizzi et al. (2017) and Huang et al. (2018). They differ from the model of Tinti et al. (2016) in which the slip is

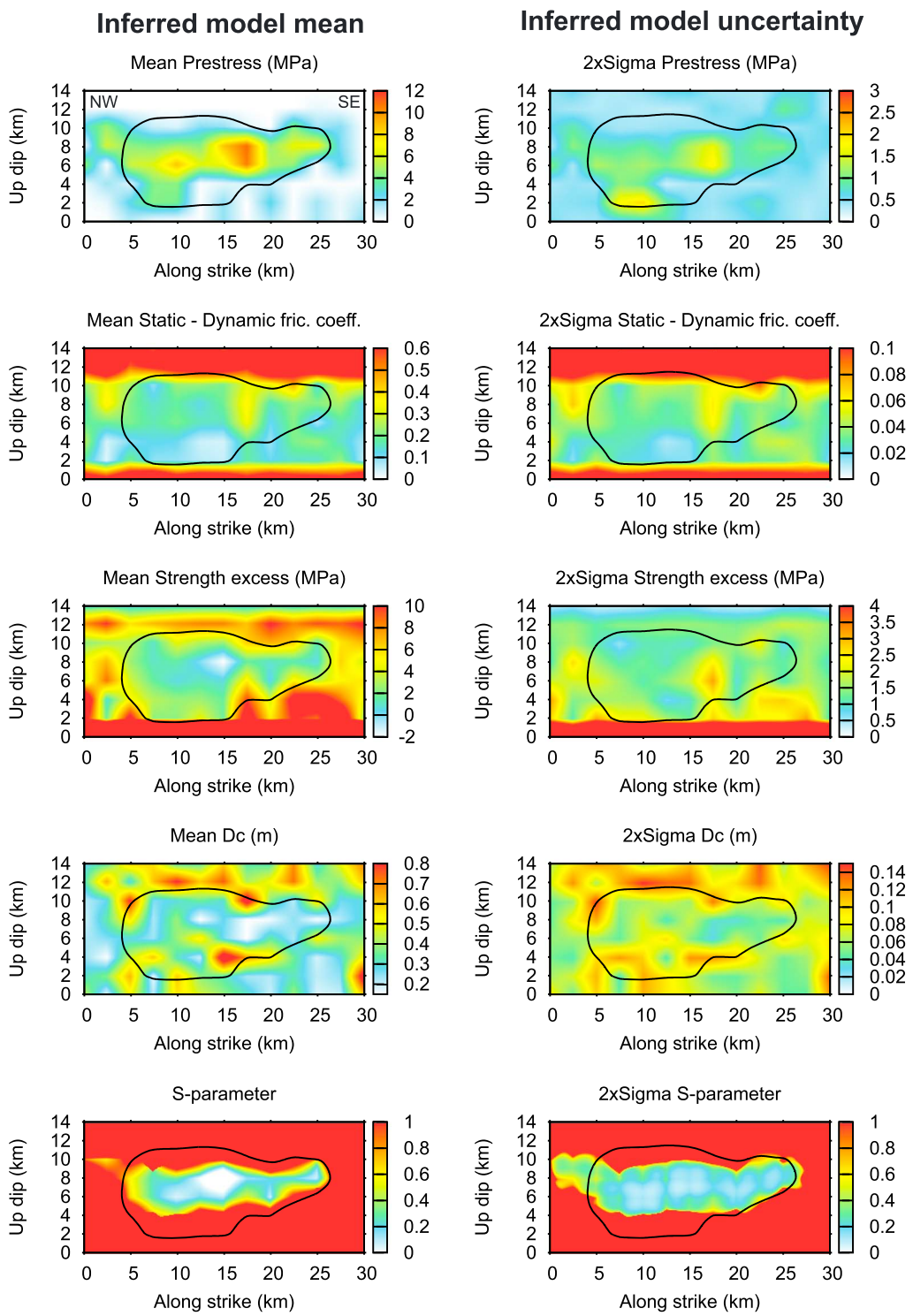

Figure 9. Distributions inferred dynamic parameters averaged over posterior samples (red) and their uncertainty in terms of two sigma. Black contour delineates the averaged slip distribution shown in Figure 8a.

composed of distinct smaller patches. Such differences among kinematic models can be attributed to the strength of smoothing constraints applied in the kinematic inversion methods. The relative smoothness of the slip distribution we obtain is, however, the result of the dynamic modeling. Indeed, in dynamic modeling of the Amatrice earthquake by Aochi and Twardzik (2019), the authors had to add smaller

rupture pathways between the NW and SE asperities in order to connect them with the nucleation patch. Therefore, a model with distinct separated slip patches would be hardly justifiable with the present friction law and model parameterization.

In terms of dynamic parameters, the slip-weighted mean stress drop falls in between 4 and 4.5 MPa, reaching locally 10 to 15 MPa. These values are consistent with stress drops inferred by Aochi and Twardzik (2019). The friction drop ranges from 0.1 to 0.4 and the characteristic slip-weakening distance varies significantly between 0.2 and 0.8 m along the fault. The radiation efficiency is estimated at ~0.2, that is, rather low, suggesting that approximately 80% of the total available energy was spent in the fracture process, while just 20% was radiated by seismic waves. Such relatively small radiation efficiency suggests relatively weak high-frequency radiation for the given magnitude. Indeed, Lanzano et al. (2016) computed between-event terms with respect to Italian ground motion prediction equations for the Amatrice earthquake (see Figure 8 therein). They demonstrate that the high-frequency between-event error is smaller than the corresponding term at low frequency, suggesting that the amount of high-frequency energy was smaller than empirically expected for the given magnitude. This is thus in agreement with our finding that the energy budget of the Amatrice earthquake rupture was dominated by the fracture process.

6.1. Weak Nucleation of the Earthquake

The inferred model of the 2016 Amatrice earthquake is characterized by a relatively weak nucleation, where the rupture almost dies out before restarting and extending to the full M_w 6.2 earthquake. Therefore, the rupture propagation is purely spontaneous in the sense that the nucleation patch did not give much "push" to the rupture onset.

Weak nucleation suggests that the eventual earthquake size is not determined at the nucleation stage. Instead, the progress of the rupture process is controlled by subtle spatial heterogeneities of the local readiness of the fault to rupture. Such character of the rupture process has important implications for the (im)possibility of prediction of the earthquake magnitude from the beginning of the observed seismograms. This in turn has implications for early warning systems (Murphy & Nielsen, 2009). Nevertheless, to test if more solid evidence for such behavior exists, systematic dynamic inversions of many other events would be needed.

6.2. Structural Control on the Earthquake Rupture

In our approach we do not distinguish between the classical asperity and barrier dynamic rupture models Di Carli et al. (2010). Due to the parameterization of the dynamic source properties the rupture can be locally stopped by low prestress, high strength, but also large D_c (where the latter two combine in large G_c). This is evident when inspecting Figure 9 for the possible role of the various dynamic parameters in constraining the rupture extent. In particular, large values of strength excess surround the rupture from the top and bottom, due to both low prestress and large friction drop. However, in the along-strike direction, the strength excess outside the rupture zone is lower. Moreover, in the NW part it has large uncertainty. Another parameter controlling rupture arrest is the characteristic slip weakening distance D_c. It is small in the SE part, suggesting that rupture stopped there dynamically due to the rather low stress drop (i.e., low prestress) providing insufficient energy for the rupture to extend.

In the NW the situation is different. While strength excess and prestress are basically constant at the NW inner edge of the rupture, D_c is larger even when taking its uncertainty into account (Figure 9). Pizzi et al. (2017) suggest that the apparent listric shape of the on-fault aftershocks is associated with the intersection of the normal fault with the Sibillini Mountains Thrust (MST) ramp. In 3-D the aftershocks delineate a spoon-like structure corresponding to the MST. The MST likely behaves as a structural barrier at depth, controlling the termination of the Amatrice earthquake rupture. This suggests that the structural complexity due to the intersection with the MST stopped the rupture in the NW, although not abruptly. This structural effect is reproduced in our dynamic model by making D_c larger.

6.3. Style of Rupture Propagation

The rise time distribution (Figure 8a) suggests that the rupture starts as a crack, with larger rise times (~4 s) in the middle of the fault. Then it continues as a pulse, with short rise times (~0.2 s). This result is supported by the uncertainty analysis.

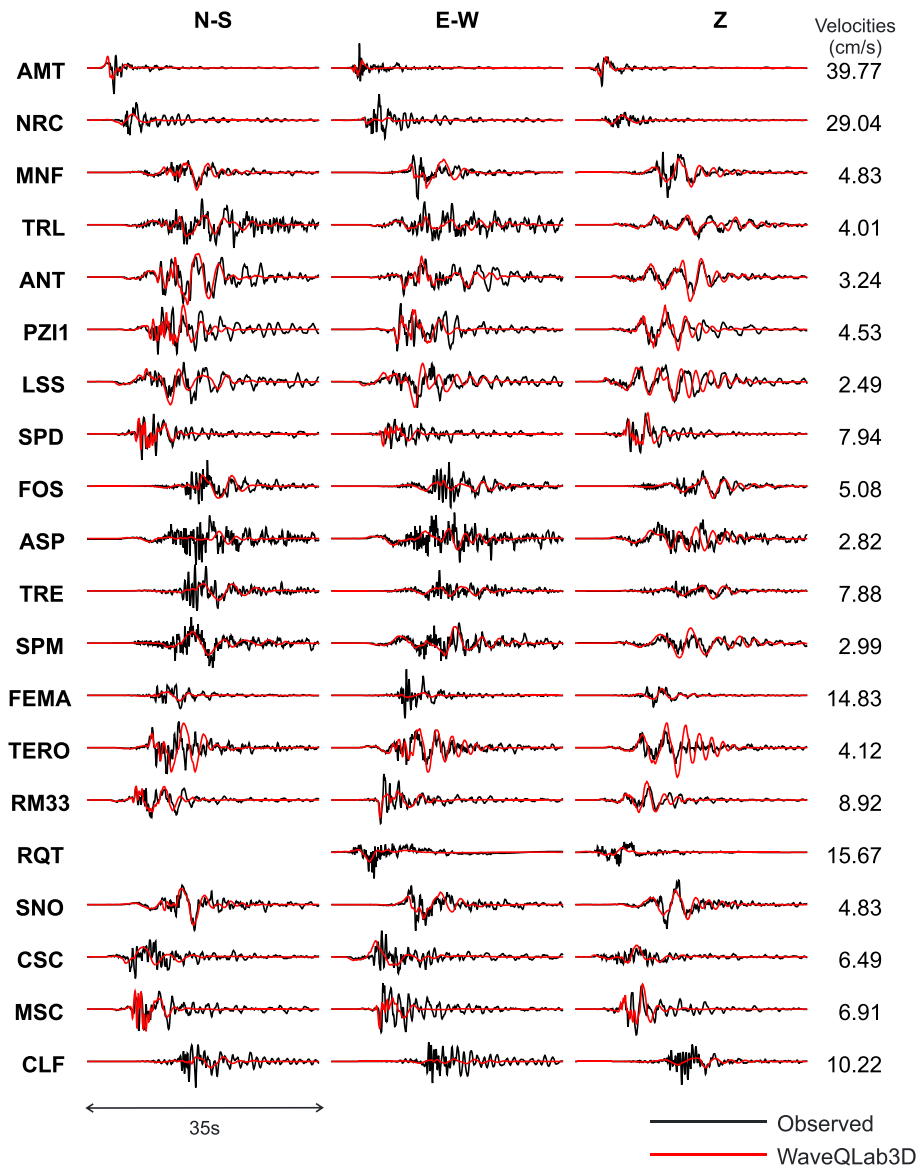

Figure 10. Comparison between observed (black) and synthetic (red) velocity waveforms for the best-fitting model of Figure 4 calculated by WaveQLab3D in frequency range 0.05–5.0 Hz. Note that there is no additional alignment time shift of the individual waveforms.

Remarkably, rupture propagation in the form of slip pulses is not naturally expected from dynamic rupture simulations that assume linear slip-weakening friction on planar faults and smoothly distributed initial stresses and frictional properties. As shown in theoretical studies by Beroza and Mikumo (1996) and Oglesby and Day (2002), pulse-like rupture in linear slip-weakening models can arise from fault heterogeneities. Therefore, both the transient nucleation and the pulse-like rupture propagation are here enabled by a sensitive balance of the inhomogeneities in the inferred stress and friction parameters making the rupture zone narrower and thus producing early stopping phases. We note that for other, more complex friction laws (such as strong-velocity weakening; e.g., Gabriel et al., 2012, 2013) and/or in the presence of structural complexity (such as damage zone effects; e.g., Huang & Ampuero, 2011, Huang et al., 2014, or geometric complexity; e.g., Wollherr et al., 2019), pulse-like rupture propagation is more typical. In this sense, the strongly inhomogeneous friction properties in our models, especially D_c, represents rather a proxy for unaccounted dynamic features. Therefore, dynamic models with geometrically complex fault geometries,

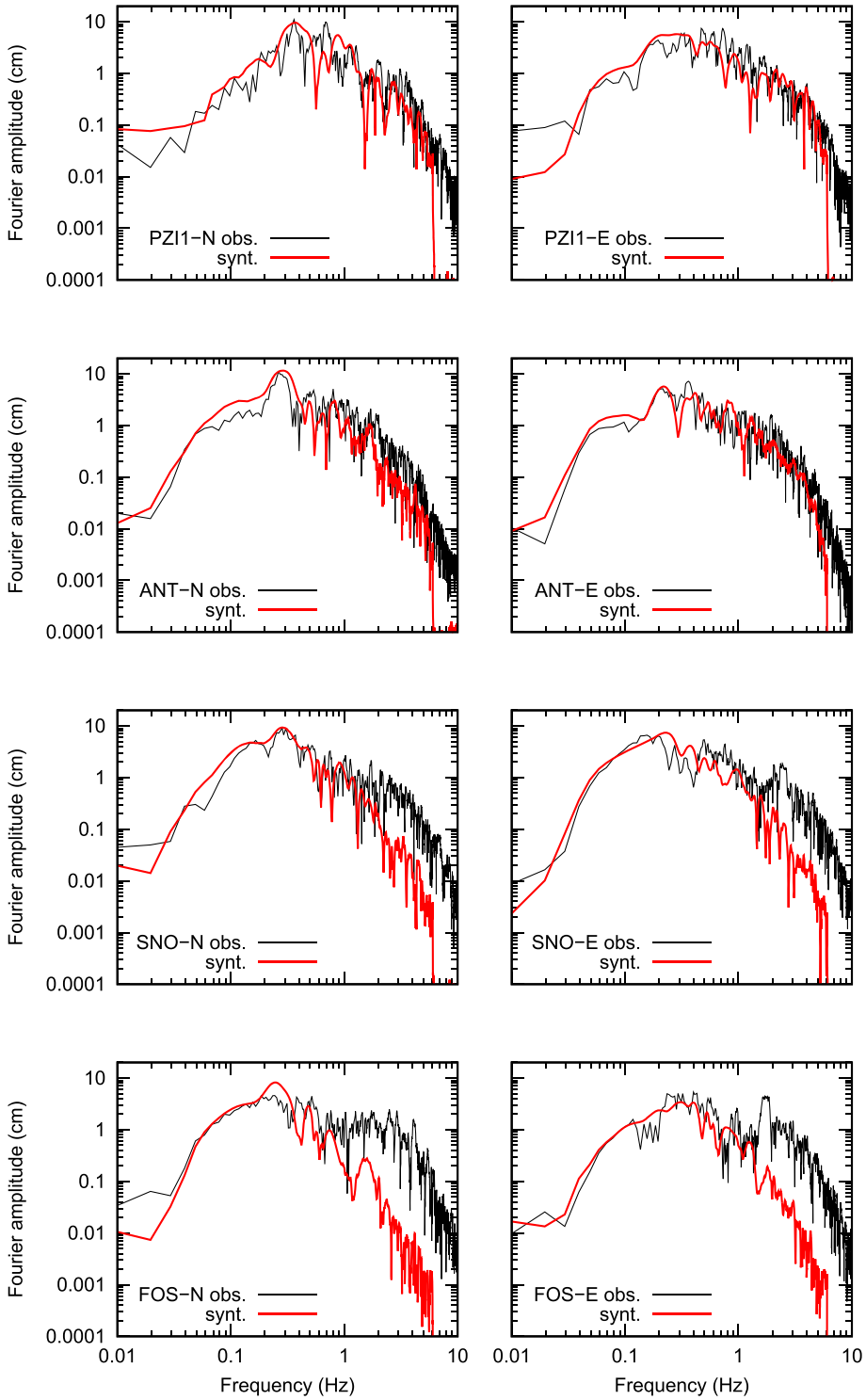

Figure 11. Comparison between Fourier spectra of observed (black) and synthetic (red) velocity waveforms for the best-fitting model of Figure 4 calculated by WaveQLab3D in frequency range 0.05–5.0 Hz for selected stations (rows) and components (columns). For comparison of their respective waveforms in time domain see Figure 10. Note that the dynamic inversion was based only on the frequency range of 0.05–1 Hz. The upper two rows represent examples of stations having presumably weak site effects. Contrarily, the bottom two are affected by site effect for frequencies larger than ~1 Hz (see the abrupt change of the spectral decay slope).

including listric and fractally rough surfaces, and other friction laws (which can generate pulses without stress heterogeneity) shall be explored in the future.

6.4. Prediction of Broadband Ground Motions

An alluring property of the dynamic modeling is that given the dynamic parameters, one can calculate the waveforms up to much higher frequencies than considered in the inversion (<1 Hz). We can then examine to what extent our dynamic model can explain broadband recordings. We calculate the waveforms from the best-fitting model in the frequency range 0.05–5.0 Hz using the WaveQLab3D code and the precalculated Green's functions in the 1-D velocity model. The comparison of velocity waveforms is displayed in Figure 10.

The fit is surprisingly good, considering the large number of stations, their almost perfect azimuthal coverage, and the richness of the waveform shapes. The fit is exceptionally good at stations with presumably weak high-frequency site effect. This is demonstrated also in Figure 11 showing comparison of the broadband seismograms in the Fourier domain for four selected stations. The first two selected stations (PZI1 and ANT) rank among the best fitted, while the other two (SNO and FOS) serve as examples of stations with clear site effects exhibited by spectral amplification above ~1 Hz. The latter feature is obviously not captured by our simplified 1-D velocity model. Interestingly, the fit is also relatively poor for the nearest stations. This can be attributed to the oversimplified rupture geometry, to which the nearest stations are most sensitive.

This exercise demonstrates the viability of fully dynamic rupture models governed by linear slip-weakening friction combined with synthetic Green's functions to explain the major characteristics of the observations at near-source distances. This supports the possibility of using dynamic models for strong motion prediction, for example, for physics-based ground motion simulations, provided correct dynamic properties are prescribed and computational cost is affordable.

7. Conclusions

We have applied a newly developed dynamic source inversion to the well-recorded 2016 M_w 6.2 Amatrice, Central Italy, earthquake, assuming a linear slip-weakening friction law on a planar fault. Generally speaking, finding the optimal distribution of dynamic parameters is computationally challenging due to the strongly nonlinear relation between model parameters and seismograms. We formulate the inverse problem in a Bayesian framework, utilizing parallel tempering MCMC approach (Sambridge, 2013) to sample the posterior probability density function. Our approach to the dynamic inversion is tractable thanks to the combination of relatively fast (yet not perfectly precise) dynamic rupture solver and the use of prior constraints on the nucleation area (to avoid running dynamic simulations for models that would provide a poor fit to the data).

In accordance with other published kinematic and dynamic models, our rupture models exhibit bilateral rupture propagation with two asperities and pronounced propagation toward the city of Amatrice. The latter feature is most likely responsible for the damaging strong motions with peak acceleration reaching 0.8 g (Fiorentino et al., 2018). The slip-weighted mean stress drop is between 4 and 4.5 MPa. The friction drop ranges from 0.1 to 0.4 and the characteristic slip-weakening distance varies significantly between 0.2 and 0.8 m along the fault. The radiation efficiency is estimated at ~0.2, suggesting that the energy budget of the Amatrice earthquake rupture was dominated by the fracture process. This explains the observed relatively weak high-frequency radiation identified from comparison with Italian ground motion prediction equations (Lanzano et al., 2016).

Since the dynamic inversion also provides kinematic parameters of the rupture, it can be also viewed as a kinematic inversion constrained by the assumed friction law. This is advisable as kinematic inversions are highly nonunique (Gallovič & Ampuero, 2015; Gallovič and Zahradník, 2011; Mai et al., 2016).

The present dynamic inversion opens an avenue for systematic analysis of a large number of earthquakes. Subsequent statistical analysis of the resulting dynamic parameters could allow to study relations between fault strength and slip to validate fault weakening models, and to dynamically constrain rupture simulations for practical applications such as seismic hazard assessment.

Appendix A: Validation of the Best Model

Here we compare rupture simulations calculated by the fast-speed FD3D code used in the inversion with the state-of-the-art code WaveQLab3D (Duru & Dunham, 2016) for the case of the best-fitting source model of the Amatrice earthquake (see Figure 6 for the distribution of its dynamic parameter distribution). WaveQLab3D solves the 3-D elastic wave equation in collocated curvilinear grids, where the spatial discretization uses high-order accurate finite difference schemes satisfying the Summation-By-Parts rule (sixth-order accurate central finite difference stencils in the interior and one-sided third-order accurate at boundaries). The time discretization uses a fourth-order accurate low-storage Runge-Kutta approach. Boundary conditions and frictional interfaces are imposed weakly using penalties, resulting in an energy-stable scheme. WaveQLab3D handles fault boundary conditions as tractions at split nodes and uses perfectly matched layers as absorbing boundaries. WaveQLab3D has been verified in many community dynamic rupture benchmarks (Harris et al., 2018). In the WaveQLab3D simulation we respect the actual fault geometry and dynamic normal stress changes. Comparing computational demands of the two codes, we find that while WaveQLab3D requires 6 hr on a recent eight-core CPU, FD3D only requires 10 min on a single-core CPU, that is, the latter being ~300 times faster.

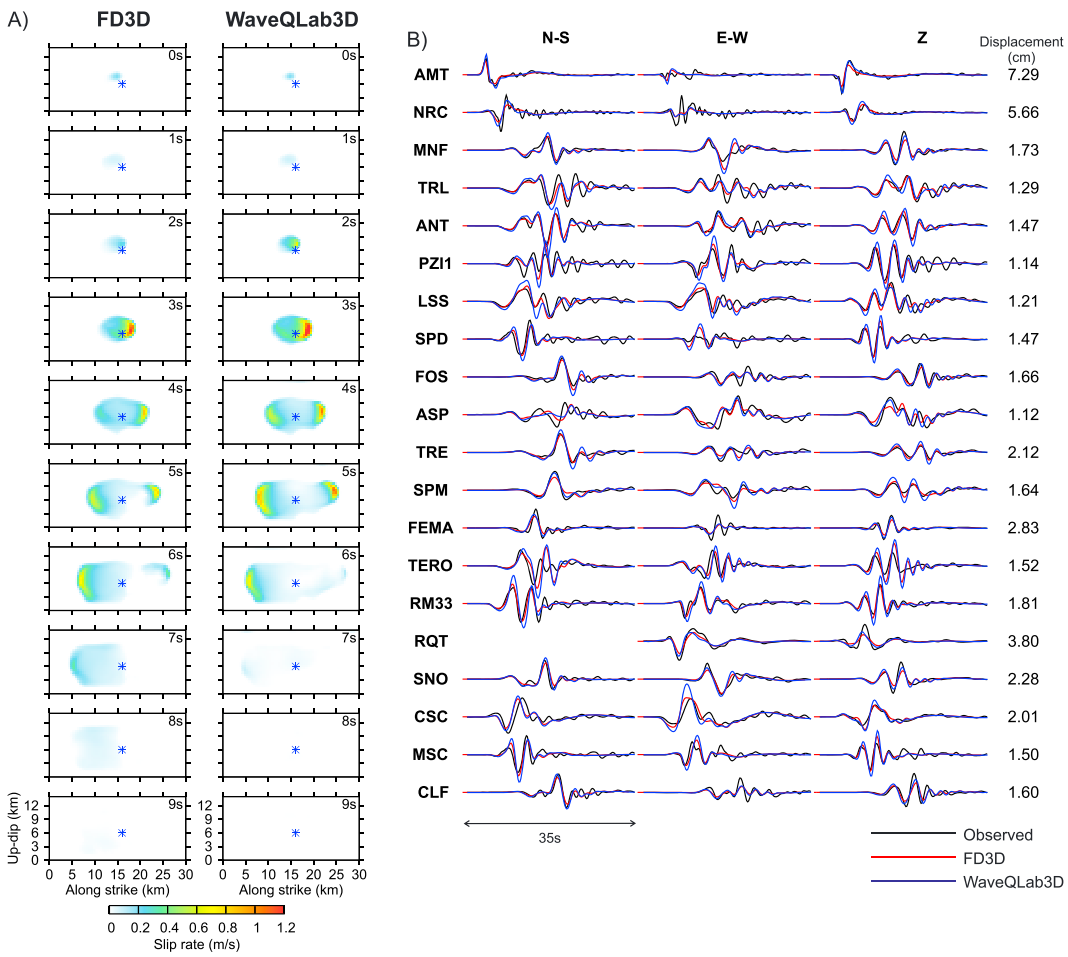

Figure A1. Validation of the best-fitting model of Figure 4 using WaveQLab3D dynamic rupture simulation code by Duru and Dunham (2016). In WaveQLab3D the dipping fault geometry and the consequent dynamic normal stress variations are fully respected in the simulation, while in the FD3D the fault is approximated by a vertical plane to speed-up the calculation. The simulation results calculated by the two codes are compared in terms of (a) slip-rate snapshots, and (b) displacement seismograms in the same frequency range as considered in the inversion (see Figure 4b). The station names are depicted on the left (for their position see Figure 1). Maximum amplitudes at the individual stations are shown on the right.

Figure A1A compares snapshots of the simulated rupture propagation. Figure A1b compares the simulated waveforms. The main features of the rupture propagation are well captured by the FD3D solver. By experimenting we have found that the essential point is the mapping of the crustal model onto the approximate vertical fault plane to respect the spatial position of velocity model interfaces along the inclined fault. Furthermore, normal stress changes that are not accounted for when considering the vertical fault geometry (in FD3D) have only very minor effect on the rupture propagation in our case, in which the rupture has not reached the surface. WaveQLab tends to provide slightly faster rupture propagation for the given distribution of the dynamic parameters (and thus slightly larger waveforms), which we attribute to a better resolution of dynamic stress changes along the rupture front. Nevertheless, considering the extreme difference in the computational demands, we consider the agreements between the two solutions as satisfactory. Regarding the simulation speed, we note that due to the relative simplicity of the FD3D code, it was straightforwardly ported to GPU using OpenACC directives, which are implemented by the Portland Fortran compiler. The additional speedup of GPU (NVIDIA GTX Titan) versus the single-core CPU is about 5 times; that is, a single complete dynamic rupture simulation is performed within approximately 2 min.

Acknowledgments
We thank L. Hanyk and J. Premus for their help with the software development, and K. Duru for providing us with the WaveQLab3D solver and for his guidance in its usage. We are grateful to Olaf Zielke and an anonymous reviewer for their valuable comments that improved the presentation of our results. The observed data were downloaded from the Engineering Strong-Motion database (Luzi, Puglia, Russo, D'Amico, et al., 2016; Luzi, Puglia, Russo, & ORFEUS WG5, 2016). Most of the calculations were carried out on Salmon supercomputer (Ostrava), supported by the Ministry of Education, Youth and Sports from the Large Infrastructures for Research, Experimental Development and Innovations project "IT4Innovations National Supercomputing Center – LM2015070" (IT4I supercomputer). F. G., L. V., and A.-A. G. acknowledge financial support through the bilateral project of the Czech Science Foundation and DFG, 18-06716J and GA 2465/2-1, respectively. J.-P. A. acknowledges support by the French government, through the UCAJEDI Investments in the Future project managed by the National Research Agency (ANR) with reference ANR-15-IDEX-01. A.-A. G. acknowledges support by the European Union's Horizon 2020 research and innovation program (ExaHyPE, grant 671698 and ChEESE, grant 823844), by the Volkswagen Foundation (ASCETE, grant 88479) and by KAUST-CRG (GAST, grant ORS-2016-CRG5-3027 and FRAGEN, grant ORS-2017-CRG6 3389.02).

References

Aki, K., & Richards, P. G. (2002). *Quantitative seismology*. Sausalito, California: University Science Books.

Ameri, G., Gallovic, F., & Pacor, F. (2012). Complexity of the *Mw* 6.3 2009 L'Aquila (Central Italy) earthquake: 2. Broadband strong-motion modeling. *Journal of Geophysical Research*, *117*, B04308. https://doi.org/10.1029/2011JB008709

Andrews, D. J. (1976). Rupture velocity of plane strain shear cracks. *Journal of Geophysical Research*, *81*(32), 5679–5687. https://doi.org/10.1029/JB081i032p05679

Aochi, H., and C. Twardzik (2019). Imaging of seismogenic asperities of the 2016 M_L 6.0 Amatrice, Central Italy, earthquake through dynamic rupture simulations, *Pure and Applied Geophysics*. https://doi.org/10.1007/s00024-019-02199-z

Beroza, G. C., & Mikumo, T. (1996). Short slip duration in dynamic rupture in the presence of heterogeneous fault properties. *Journal of Geophysical Research*, *101*(B10), 22,449–22,460. https://doi.org/10.1029/96JB02291

Bindi, D., Spallarossa, D., Picozzi, M., Scafidi, D., & Cotton, F. (2018). Impact of magnitude selection on aleatory variability associated with ground-motion prediction equations: Part I—Local, energy, and moment magnitude calibration and stress-drop variability in Central Italy. *Bulletin of the Seismological Society of America*, *108*(3A), 1427–1442. https://doi.org/10.1785/0120170356

Bouchon, M. (1981). A simple method to calculate Green's functions for elastic layered media. *Bulletin of the Seismological Society of America*, *71*, 959–971.

Cheloni, D., de Novellis, V., Albano, M., Antonioli, A., Anzidei, M., Atzori, S., et al. (2017). Geodetic model of the 2016 Central Italy earthquake sequence inferred from InSAR and GPS data. *Geophysical Research Letters*, *44*, 6778–6787. https://doi.org/10.1002/2017GL073580

Chiaraluce, L., di Stefano, R., Tinti, E., Scognamiglio, L., Michele, M., Casarotti, E., et al. (2017). The 2016 Central Italy seismic sequence: A first look at the mainshocks, aftershocks, 652 and source models. *Seismological Research Letters*, *88*(3), 757–771. https://doi.org/10.1785/0220160221

Cirella, A., Pezzo, G., & Piatanesi, A. (2018). Rupture kinematics and structural-rheological control of the2016 M_w 6.1 Amatrice (central Italy) earthquake from joint inversion of seismic and geodetic data. *Geophysical Research Letters*, *45*, 12,302–12,311. https://doi.org/10.1029/2018GL080894

Corish, S. M., Bradley, C. R., & Olsen, K. B. (2007). Assessment of a nonlinear dynamic rupture inversion technique applied to a synthetic earthquake. *Bulletin of the Seismological Society of America*, *97*(3), 901–914. https://doi.org/10.1785/0120060066

Coutant, O. (1989). Program of numerical simulation AXITRA, Tech. rep., Lab. de Geophys. Interne et Tectonophys., Grenoble, France.

Di Carli, S., François-Holden, C., Peyrat, S., & Madariaga, R. (2010). Dynamic inversion of the 2000 Tottori earthquake based on elliptical subfault approximations. *Journal of Geophysical Research*, *125*, B12328. https://doi.org/10.1029/2009JB006358

Dunham, E. M. (2007). Conditions governing the occurrence of supershear ruptures under slip-weakening friction. *Journal of Geophysical Research*, *112*, B07302. https://doi.org/10.1029/2006JB004717

Duru, K., & Dunham, E. M. (2016). Dynamic earthquake rupture simulations on nonplanar faults embedded in 3D geometrically complex, heterogeneous Earth models. *Journal of Computational Physics*, *305*, 185–207. https://doi.org/10.1016/j.jcp.2015.10.021

Falcioni, M., & Deem, M. W. (1999). A biased Monte Carlo scheme for zeolite structure solution. *The Journal of Chemical Physics*, *110*(3), 1754–1766. https://doi.org/10.1063/1.477812

Fiorentino, G., Forte, A., Pagano, E., Sabetta, F., Baggio, C., Lavorato, D., et al. (2018). Damage patterns in the town of Amatrice after August 24th 2016 Central Italy earthquakes. *Bulletin of Earthquake Engineering*, *16*(3), 1399–1423. https://doi.org/10.1007/s10518-017-0254-z

Fukuyama, E., & Mikumo, T. (1993). Dynamic rupture analysis: Inversion for the source process of the 1990 Izu-Oshima, Japan, earthquake. *Journal of Geophysical Research*, *98*(B4), 6529–6542. https://doi.org/10.1029/92JB02451

Gabriel, A. A., Ampuero, J. P., Dalguer, L. A., & Mai, P. M. (2012). The transition of dynamic rupture styles in elastic media under velocity-weakening friction. *Journal of Geophysical Research*, *117*, B09311. https://doi.org/10.1029/2012JB009468

Gabriel, A.-A., Ampuero, J.-P., Dalguer, L. A., & Mai, P. M. (2013). Source properties of dynamic rupture pulses with off-fault plasticity. *Journal of Geophysical Research: Solid Earth*, *118*, 4117–4126. https://doi.org/10.1029/2012JB009468

Gallovič, F., & Ampuero, J.-P. (2015). A new strategy to compare inverted rupture models exploiting the eigen-structure of the inverse problem. *Seismological Research Letters*, *86*(6), 1679–1689. https://doi.org/10.1785/0220150096

Gallovič, F., Imperatori, W., & Mai, P. M. (2015). Effects of three-dimensional crustal structure and smoothing constraint on earthquake slip inversions: Case study of the M_w 6.3 2009 L'Aquila earthquake. *Journal of Geophysical Research: Solid Earth*, *120*, 428–449. https://doi.org/10.1002/2014JB011650

Gallovič, F., Valentová, Ľ., Ampuero, J.-P., & Gabriel, A.-A. (2019). Bayesian dynamic finite-fault inversion: 1. Method and synthetic test. *Journal of Geophysical Research: Solid Earth*, *124*, 6949–6969. https://doi.org/10.1029/2019JB017510

Gallovič, F., & Zahradník, J. (2011). Toward understanding slip-inversion uncertainty and artifacts: 2. Singular value analysis, *Journal of Geophysical Research*, *116*, B02309. https://doi.org/10.1029/2010JB007814

Gallovič, F., & Zahradník, J. (2012). Complexity of the Mw 6.3 2009 L'Aquila (Central Italy) earthquake: 1. Multiple finite-extent source inversion. *Journal of Geophysical Research*, *117*, B04307. https://doi.org/10.1029/2011JB008709

Hallo, M., & Gallovič, F. (2016). Fast and cheap approximation of Green functions uncertainty for waveform-based earthquake source inversions. *Geophysical Journal International*, *207*(2), 1012–1029. https://doi.org/10.1093/gji/ggw320

Harris, R. A., Barall, M., Aagaard, B. T., Ma, S., Roten, D., Olsen, K. B., et al. (2018). A suite of exercises for verifying dynamic earthquake rupture codes. *Seismological Research Letters*, *89*(3), 1146–1162. https://doi.org/10.1785/0220170222

Huang, M.-H., Fielding, E. J., Liang, C., Milillo, P., Bekaert, D., Dreger, D., & Salzer, J. (2017). Coseismic deformation and triggered landslides of the 2016 M_w 6.2 Amatrice earthquake in Italy. *Geophysical Research Letters*, *44*, 1266–1274. https://doi.org/10.1002/2016GL071687

Huang, Y., & Ampuero, J.-P. (2011). Pulse-like ruptures induced by low-velocity fault zones. *Journal of Geophysical Research*, *116*, B12307. https://doi.org/10.1029/2011JB008684

Huang, Y., Ampuero, J. P., & Helmberger, D. V. (2014). Earthquake ruptures modulated by waves in damaged fault zones. *Journal of Geophysical Research: Solid Earth*, *119*, 3133–3154. https://doi.org/10.1002/2013JB010724

Kanamori, H., & Brodsky, E. E. (2004). The physics of earthquakes. *Reports on Progress in Physics*, *67*(8), 1429–1496. https://doi.org/10.1088/0034-4885/67/8/R03

Kennett, B. L. N., & Kerry, N. J. (1979). Seismic waves in a stratified half space. *Geophysical Journal International*, *57*(3), 557–583. https://doi.org/10.1111/j.1365-246X.1979.tb06779.x

Lanzano, G., Luzi, L., Pacor, F., Puglia, R., D'Amico, M., Felicetta, C., & Russo, E. (2016). Preliminary analysis of the accelerometric recordings of the August 24th, 2016 M_w 6.0 Amatrice earthquake. *Annales de Geophysique*, *59*, 1–7. https://doi.org/10.4401/ag-7201

Luzi, L., Puglia, R., Russo, E., D'Amico, M., Felicetta, C., Pacor, F., et al. (2016). The Engineering Strong-Motion database: A platform to access Pan-European accelerometric data. *Seismological Research Letters*, *87*(4), 987–997. https://doi.org/10.1785/0220150278

Luzi, L., Puglia, R., Russo, E., & ORFEUS WG5 (2016). Engineering Strong Motion Database, version 1.0, Istituto Nazionale di Geofisica e Vulcanologia. Observatories & Research Facilities for European Seismology. https://doi.org/10.13127/ESM

Madariaga, R., Olsen, K. B., & Archuleta, R. J. (1998). Modelling dynamic rupture in a 3D earthquake fault model. *Bulletin of the Seismological Society of America*, *88*, 1182–1197.

Mai, P. M., Schorlemmer, D., Page, M., Ampuero, J.-P., Asano, K., Causse, M., et al. (2016). The earthquake-source inversion validation (SIV) project. *Seismological Research Letters*, *87*(3), 690–708. https://doi.org/10.1785/0220150231

Murphy, S., & Nielsen, S. (2009). Estimating earthquake magnitude with early arrivals: A test using dynamic and kinematic models. *Bulletin of the Seismological Society of America*, *99*(1), 1–23. https://doi.org/10.1785/0120070246

Oglesby, D. D., & Day, S. M. (2002). Stochastic fault stress: Implications for fault dynamics and ground motion. *Bulletin of the Seismological Society of America*, *92*(8), 3006–3021. https://doi.org/10.1785/0120010249

Okada, Y. (1992). Internal deformation due to shear and tensile faults in a half-space. *Bulletin of the Seismological Society of America*, *82*, 1018–1040.

Pacor, F., Spallarossa, D., Oth, A., Luzi, L., Puglia, R., Cantore, L., et al. (2016). Spectral models for ground motion prediction in the L'Aquila region (central Italy): Evidence for stress-drop dependence on magnitude and depth. *Geophysical Journal International*, *204*(2), 697–718. http://doi.org/10.1093/gji/ggv448

Peyrat, S., & Olsen, K. B. (2004). Nonlinear dynamic rupture inversion of the 2000 Western Tottori, Japan, earthquake. *Geophysical Research Letters*, *31*, L05604. https://doi.org/10.1029/2003GL019058

Pizzi, A., Di Domenica, A., Gallovič, F., Luzi, L., & Puglia, R. (2017). Fault segmentation as constraint to the occurrence of the main shocks of the 2016 Central Italy seismic sequence. *Tectonics*, *36*, 2370–2387. https://doi.org/10.1002/2017TC004652

Ragon, T., Sladen, A., & Simons, M. (2018). Accounting for uncertain fault geometry in earthquake source inversions—I: Theory and simplified application. *Geophysical Journal International*, *214*(2), 1174–1190. https://doi.org/10.1093/gji/ggy187

Ragon, T., Sladen, A., & Simons, M. (2019). Accounting for uncertain fault geometry in earthquake source inversions—II: Application to the M_w 6.2 Amatrice earthquake, central Italy. *Geophysical Journal International*, *218*(1), 689–707. https://doi.org/10.1093/gji/ggz180

Ren, Y., Wang, H., & Wen, R. (2017). Imprint of rupture directivity from ground motions of the 24 August 2016 M_w6.2 Central Italy earthquake. *Tectonics*, *36*, 3178–3191. https://doi.org/10.1002/2017TC004673

Ripperger, J., Ampuero, J.-P., Mai, M. P., & Giardini, D. (2007). Earthquake source characteristics from dynamic rupture with constrained stochastic fault stress. *Journal of Geophysical Research*, *112*, B04311. https://doi.org/10.1029/2006JB004515

Ruiz, S., & Madariaga, R. (2011). Determination of the friction law parameters of the M_w 6.7 Michilla earthquake in northern Chile by dynamic inversion. *Geophysical Research Letters*, *38*, L09317. https://doi.org/10.1029/2011GL047147

Sambridge, M. (2013). A parallel tempering algorithm for probabilistic sampling and multimodal optimization. *Geophysical Journal International*, *196*, 357–374.

Tinti, E., Scognamiglio, L., Michelini, A., & Cocco, M. (2016). Slip heterogeneity and directivity of the ML 6.0, 2016, Amatrice earthquake estimated with rapid finite-fault inversion. *Geophysical Research Letters*, *43*, 10,745–10,752. https://doi.org/10.1002/2016GL071263

Tung, S., & Masterlark, T. (2018). Resolving source geometry of the 24 August 2016 Amatrice, Central Italy, earthquake from InSAR data and 3D finite-element modeling. *Bulletin of the Seismological Society of America*, *108*(2), 553–572. https://doi.org/10.1785/0120170139

Twardzik, C., Das, S., & Madariaga, R. (2014). Inversion for the physical parameters that control the source dynamics of the 2004 Parkfield earthquake. *Journal of Geophysical Research: Solid Earth*, *119*, 7010–7027. https://doi.org/10.1002/2014JB011238

Ulrich, T., Gabriel, A. A., Ampuero, J. P., & Xu, W. (2019). Dynamic viability of the 2016 *Mw* 7.8 Kaikoura earthquake cascade on weak crustal faults. *Nature Communications*, *10*(1), 1213. https://doi.org/10.1038/s41467-019-09125-w

Viesca, R. C., & Garagash, D. I. (2015). Ubiquitous weakening of faults due to thermal pressurization. *Nature Geoscience*, *8*(11), 875–879. https://doi.org/10.1038/ngeo2554

Wollherr, S., Gabriel, A.-A., & Mai, P. M. (2019). Landers 1992 "reloaded": Integrative dynamic earthquake rupture modeling. *Journal of Geophysical Research: Solid Earth*, *124*. https://doi.org/10.1029/2018JB016355